

Influences of tissue absorption and scattering on diffuse correlation spectroscopy blood flow measurements

Daniel Irwin,¹ Lixin Dong,¹ Yu Shang,¹ Ran Cheng,¹ Mahesh Kudrimoti,² Scott D. Stevens,³ and Guoqiang Yu^{1*}

¹Center for Biomedical Engineering, University of Kentucky, Lexington, KY 40506, USA

²Department of Radiation Medicine, University of Kentucky Chandler Hospital, Lexington, KY 40536, USA

³Department of Radiology, University of Kentucky Chandler Hospital, Lexington, KY 40536, USA

*guoqiang.yu@uky.edu

Abstract: In this study we evaluate the influences of optical property assumptions on near-infrared diffuse correlation spectroscopy (DCS) flow index measurements. The optical properties, absorption coefficient (μ_a) and reduced scattering coefficient (μ_s'), are independently varied using liquid phantoms and measured concurrently with the flow index using a hybrid optical system combining a dual-wavelength DCS flow device with a commercial frequency-domain tissue-oximeter. DCS flow indices are calculated at two wavelengths (785 and 830 nm) using measured μ_a and μ_s' or assumed constant μ_a and μ_s' . Inaccurate μ_s' assumptions resulted in much greater flow index errors than inaccurate μ_a . Underestimated/overestimated μ_s' from $-35\%/+175\%$ lead to flow index errors of $+110\%/-80\%$, whereas underestimated/overestimated μ_a from $-40\%/+150\%$ lead to $-20\%/+40\%$, regardless of the wavelengths used. Examination of a clinical study involving human head and neck tumors indicates up to $+280\%$ flow index errors resulted from inter-patient optical property variations. These findings suggest that studies involving significant μ_a and μ_s' changes should concurrently measure flow index and optical properties for accurate extraction of blood flow information.

© 2011 Optical Society of America

OCIS codes: (170.0170) Medical optics and biotechnology; (170.3660) Light propagation in tissues; (170.3880) Medical and biological imaging; (170.6480) Spectroscopy, speckle.

References and links

1. D. A. Boas, L. E. Campbell, and A. G. Yodh, "Scattering and imaging with diffusing temporal field correlations," *Phys. Rev. Lett.* **75**(9), 1855–1858 (1995).
2. D. A. Boas, "Diffuse photon probes of structural and dynamical properties of turbid media: theory and biomedical applications," Ph.D. dissertation (University of Pennsylvania, 1996).
3. D. A. Boas and A. G. Yodh, "Spatially varying dynamical properties of turbid media probed with diffusing temporal light correlation," *J. Opt. Soc. Am. A* **14**(1), 192–215 (1997).
4. C. Cheung, J. P. Culver, K. Takahashi, J. H. Greenberg, and A. G. Yodh, "*In vivo* cerebrovascular measurement combining diffuse near-infrared absorption and correlation spectroscopies," *Phys. Med. Biol.* **46**(8), 2053–2065 (2001).
5. J. Li, G. Dietsche, D. Iftime, S. E. Skipetrov, G. Maret, T. Elbert, B. Rockstroh, and T. Gisler, "Noninvasive detection of functional brain activity with near-infrared diffusing-wave spectroscopy," *J. Biomed. Opt.* **10**(4), 044002 (2005).
6. F. Jaillon, J. Li, G. Dietsche, T. Elbert, and T. Gisler, "Activity of the human visual cortex measured non-invasively by diffusing-wave spectroscopy," *Opt. Express* **15**(11), 6643–6650 (2007).
7. T. Durduran, "Non-invasive measurements of tissue hemodynamics with hybrid diffuse optical methods," Ph.D. dissertation (University of Pennsylvania, 2004).
8. E. M. Buckley, N. M. Cook, T. Durduran, M. N. Kim, C. Zhou, R. Choe, G. Yu, S. Schultz, C. M. Sehgal, D. J. Licht, P. H. Arger, M. E. Putt, H. H. Hurt, and A. G. Yodh, "Cerebral hemodynamics in preterm infants during

- positional intervention measured with diffuse correlation spectroscopy and transcranial Doppler ultrasound,” *Opt. Express* **17**(15), 12571–12581 (2009).
9. N. Roche-Labarbe, S. A. Carp, A. Surova, M. Patel, D. A. Boas, P. E. Grant, and M. A. Franceschini, “Noninvasive optical measures of CBV, StO₂, CBF index, and rCMRO₂ in human premature neonates’ brains in the first six weeks of life,” *Hum. Brain Mapp.* **31**(3), 341–352 (2010).
 10. C. Menon, G. M. Polin, I. Prabhakaran, A. Hsi, C. Cheung, J. P. Culver, J. F. Pingpank, C. S. Sehgal, A. G. Yodh, D. G. Buerk, and D. L. Fraker, “An integrated approach to measuring tumor oxygen status using human melanoma xenografts as a model,” *Cancer Res.* **63**(21), 7232–7240 (2003).
 11. G. Yu, T. Durduran, C. Zhou, H. W. Wang, M. E. Putt, H. M. Saunders, C. M. Sehgal, E. Glatstein, A. G. Yodh, and T. M. Busch, “Noninvasive monitoring of murine tumor blood flow during and after photodynamic therapy provides early assessment of therapeutic efficacy,” *Clin. Cancer Res.* **11**(9), 3543–3552 (2005).
 12. M. N. Kim, T. Durduran, S. Frangos, B. L. Edlow, E. M. Buckley, H. E. Moss, C. Zhou, G. Yu, R. Choe, E. Maloney-Wilensky, R. L. Wolf, M. S. Grady, J. H. Greenberg, J. M. Levine, A. G. Yodh, J. A. Detre, and W. A. Kofke, “Noninvasive measurement of cerebral blood flow and blood oxygenation using near-infrared and diffuse correlation spectroscopies in critically brain-injured adults,” *Neurocrit. Care* **12**(2), 173–180 (2010).
 13. C. Zhou, S. A. Eucker, T. Durduran, G. Yu, J. Ralston, S. H. Friess, R. N. Ichord, S. S. Margulies, and A. G. Yodh, “Diffuse optical monitoring of hemodynamic changes in piglet brain with closed head injury,” *J. Biomed. Opt.* **14**(3), 034015 (2009).
 14. T. Durduran, G. Yu, M. G. Burnett, J. A. Detre, J. H. Greenberg, J. Wang, C. Zhou, and A. G. Yodh, “Diffuse optical measurement of blood flow, blood oxygenation, and metabolism in a human brain during sensorimotor cortex activation,” *Opt. Lett.* **29**(15), 1766–1768 (2004).
 15. G. Yu, T. F. Floyd, T. Durduran, C. Zhou, J. J. Wang, J. A. Detre, and A. G. Yodh, “Validation of diffuse correlation spectroscopy for muscle blood flow with concurrent arterial spin labeled perfusion MRI,” *Opt. Express* **15**(3), 1064–1075 (2007).
 16. J. P. Culver, T. Durduran, D. Furuya, C. Cheung, J. H. Greenberg, and A. G. Yodh, “Diffuse optical tomography of cerebral blood flow, oxygenation, and metabolism in rat during focal ischemia,” *J. Cereb. Blood Flow Metab.* **23**(8), 911–924 (2003).
 17. J. Li, M. Ninck, L. Koban, T. Elbert, J. Kissler, and T. Gisler, “Transient functional blood flow change in the human brain measured noninvasively by diffusing-wave spectroscopy,” *Opt. Lett.* **33**(19), 2233–2235 (2008).
 18. G. Dietsche, M. Ninck, C. Ortolfo, J. Li, F. Jaillon, and T. Gisler, “Fiber-based multispeckle detection for time-resolved diffusing-wave spectroscopy: characterization and application to blood flow detection in deep tissue,” *Appl. Opt.* **46**(35), 8506–8514 (2007).
 19. U. Sunar, H. Quon, T. Durduran, J. Zhang, J. Du, C. Zhou, G. Yu, R. Choe, A. Kilger, R. Lustig, L. Loevner, S. Nioka, B. Chance, and A. G. Yodh, “Noninvasive diffuse optical measurement of blood flow and blood oxygenation for monitoring radiation therapy in patients with head and neck tumors: a pilot study,” *J. Biomed. Opt.* **11**(6), 064021 (2006).
 20. C. Zhou, R. Choe, N. Shah, T. Durduran, G. Yu, A. Durkin, D. Hsiang, R. Mehta, J. Butler, A. Cerussi, B. J. Tromberg, and A. G. Yodh, “Diffuse optical monitoring of blood flow and oxygenation in human breast cancer during early stages of neoadjuvant chemotherapy,” *J. Biomed. Opt.* **12**(5), 051903 (2007).
 21. D. T. Ubbink, P. J. Kitslaar, J. H. Tordoir, R. S. Reneman, and M. J. Jacobs, “Skin microcirculation in diabetic and non-diabetic patients at different stages of lower limb ischaemia,” *Eur. J. Vasc. Surg.* **7**(6), 659–6 (1993).
 22. E. Wahlberg, P. Olofsson, J. Swedenborg, and B. Fagrell, “Level of arterial obstruction in patients with peripheral arterial occlusive disease (PAOD) determined by laser Doppler fluxmetry,” *Eur. J. Vasc. Surg.* **7**(6), 684–689 (1993).
 23. R. Bonner and R. Nossal, “Model for laser Doppler measurements of blood flow in tissue,” *Appl. Opt.* **20**(12), 2097–2107 (1981).
 24. Z. Chen, T. E. Milner, D. Dave, and J. S. Nelson, “Optical Doppler tomographic imaging of fluid flow velocity in highly scattering media,” *Opt. Lett.* **22**(1), 64–66 (1997).
 25. L. Li, K. Maslov, G. Ku, and L. V. Wang, “Three-dimensional combined photoacoustic and optical coherence microscopy for *in vivo* microcirculation studies,” *Opt. Express* **17**(19), 16450–16455 (2009).
 26. R. K. Wang and L. An, “Doppler optical micro-angiography for volumetric imaging of vascular perfusion *in vivo*,” *Opt. Express* **17**(11), 8926–8940 (2009).
 27. C. Zhou, G. Yu, D. Furuya, J. H. Greenberg, A. G. Yodh, and T. Durduran, “Diffuse optical correlation tomography of cerebral blood flow during cortical spreading depression in rat brain,” *Opt. Express* **14**(3), 1125–1144 (2006).
 28. M. Belau, M. Ninck, G. Hering, L. Spinelli, D. Contini, A. Torricelli, and T. Gisler, “Noninvasive observation of skeletal muscle contraction using near-infrared time-resolved reflectance and diffusing-wave spectroscopy,” *J. Biomed. Opt.* **15**(5), 057007 (2010).
 29. T. Durduran, R. Choe, G. Yu, C. Zhou, J. C. Tchou, B. J. Czerniecki, and A. G. Yodh, “Diffuse optical measurement of blood flow in breast tumors,” *Opt. Lett.* **30**(21), 2915–2917 (2005).
 30. G. Yu, T. Durduran, G. Lech, C. Zhou, B. Chance, E. R. Mohler 3rd, and A. G. Yodh, “Time-dependent blood flow and oxygenation in human skeletal muscles measured with noninvasive near-infrared diffuse optical spectroscopies,” *J. Biomed. Opt.* **10**(2), 024027 (2005).
 31. Y. Shang, Y. Zhao, R. Cheng, L. Dong, D. Irwin, and G. Yu, “Portable optical tissue flow oximeter based on diffuse correlation spectroscopy,” *Opt. Lett.* **34**(22), 3556–3558 (2009).

32. Y. Shang, T. B. Symons, T. Durduran, A. G. Yodh, and G. Yu, "Effects of muscle fiber motion on diffuse correlation spectroscopy blood flow measurements during exercise," *Biomed. Opt. Express* **1**(2), 500–511 (2010).
33. G. Yu, Y. Shang, Y. Zhao, R. Cheng, L. Dong, and S. P. Saha, "Intraoperative evaluation of revascularization effect on ischemic muscle hemodynamics using near-infrared diffuse optical spectroscopies," *J. Biomed. Opt.* **16**(2), 027004 (2011).
34. T. M. Busch, X. M. Xing, G. Yu, A. Yodh, E. P. Wileyto, H. W. Wang, T. Durduran, T. C. Zhu, and K. K. H. Wang, "Fluence rate-dependent intratumor heterogeneity in physiologic and cytotoxic responses to Photofrin photodynamic therapy," *Photochem. Photobiol. Sci.* **8**(12), 1683–1693 (2009).
35. U. Sunar, S. Makonnen, C. Zhou, T. Durduran, G. Yu, H. W. Wang, W. M. F. Lee, and A. G. Yodh, "Hemodynamic responses to antivascular therapy and ionizing radiation assessed by diffuse optical spectroscopies," *Opt. Express* **15**(23), 15507–15516 (2007).
36. G. Yu, T. Durduran, C. Zhou, T. C. Zhu, J. C. Finlay, T. M. Busch, S. B. Malkowicz, S. M. Hahn, and A. G. Yodh, "Real-time in situ monitoring of human prostate photodynamic therapy with diffuse light," *Photochem. Photobiol.* **82**(5), 1279–1284 (2006).
37. T. Durduran, C. Zhou, E. M. Buckley, M. N. Kim, G. Yu, R. Choe, J. W. Gaynor, T. L. Spray, S. M. Durning, S. E. Mason, L. M. Montenegro, S. C. Nicolson, R. A. Zimmerman, M. E. Putt, J. Wang, J. H. Greenberg, J. A. Detre, A. G. Yodh, and D. J. Licht, "Optical measurement of cerebral hemodynamics and oxygen metabolism in neonates with congenital heart defects," *J. Biomed. Opt.* **15**(3), 037004 (2010).
38. L. Koban, M. Ninck, J. Li, T. Gisler, and J. Kissler, "Processing of emotional words measured simultaneously with steady-state visually evoked potentials and near-infrared diffusing-wave spectroscopy," *BMC Neurosci.* **11**(1), 85 (2010).
39. B. L. Edlow, M. N. Kim, T. Durduran, C. Zhou, M. E. Putt, A. G. Yodh, J. H. Greenberg, and J. A. Detre, "The effects of healthy aging on cerebral hemodynamic responses to posture change," *Physiol. Meas.* **31**(4), 477–495 (2010).
40. T. Durduran, C. Zhou, B. L. Edlow, G. Yu, R. Choe, M. N. Kim, B. L. Cucchiara, M. E. Putt, Q. Shah, S. E. Kasner, J. H. Greenberg, A. G. Yodh, and J. A. Detre, "Transcranial optical monitoring of cerebrovascular hemodynamics in acute stroke patients," *Opt. Express* **17**(5), 3884–3902 (2009).
41. Y. Shang, R. Cheng, L. Dong, S. J. Ryan, S. P. Saha, and G. Yu, "Cerebral monitoring during carotid endarterectomy using near-infrared diffuse optical spectroscopies and electroencephalogram," *Phys. Med. Biol.* **56**(10), 3015–3032 (2011).
42. M. Ninck, M. Untenberger, and T. Gisler, "Diffusing-wave spectroscopy with dynamic contrast variation: disentangling the effects of blood flow and extravascular tissue shearing on signals from deep tissue," *Biomed. Opt. Express* **1**(5), 1502–1513 (2010).
43. R. C. Mesquita, N. Skuli, M. N. Kim, J. Liang, S. Schenkel, A. J. Majmundar, M. C. Simon, and A. G. Yodh, "Hemodynamic and metabolic diffuse optical monitoring in a mouse model of hindlimb ischemia," *Biomed. Opt. Express* **1**(4), 1173–1187 (2010).
44. S. Fantini, M. A. Franceschini, and E. Gratton, "Semi-infinite-geometry boundary-problem for light migration in highly scattering media - a frequency-domain study in the diffusion-approximation," *J. Opt. Soc. Am. B* **11**(10), 2128–2138 (1994).
45. D. Wallace, B. Michener, D. Choudhury, M. Levi, P. Fennelly, D. Hueber, and B. Barbieri, "Summary of the results of a 95 subject human clinical trial for the diagnosis of peripheral vascular disease using a near infrared frequency domain hemoglobin spectrometer," *Proc. SPIE* **3597**, 300–316 (1999).
46. C. Zhou, "*In-vivo* optical imaging and spectroscopy of cerebral hemodynamics," Ph.D. dissertation (University of Pennsylvania, 2007).
47. F. Jaillon, S. E. Skipetrov, J. Li, G. Dietsche, G. Maret, and T. Gisler, "Diffusing-wave spectroscopy from head-like tissue phantoms: influence of a non-scattering layer," *Opt. Express* **14**(22), 10181–10194 (2006).
48. J. P. Culver, R. Choe, M. J. Holboke, L. Zubkov, T. Durduran, A. Slemp, V. Ntziachristos, B. Chance, and A. G. Yodh, "Three-dimensional diffuse optical tomography in the parallel plane transmission geometry: evaluation of a hybrid frequency domain/continuous wave clinical system for breast imaging," *Med. Phys.* **30**(2), 235–247 (2003).
49. D. A. Boas, J. P. Culver, J. J. Stott, and A. K. Dunn, "Three dimensional Monte Carlo code for photon migration through complex heterogeneous media including the adult human head," *Opt. Express* **10**(3), 159–170 (2002).
50. L. Gagnon, M. Desjardins, J. Jehanne-Lacasse, L. Bherer, and F. Lesage, "Investigation of diffuse correlation spectroscopy in multi-layered media including the human head," *Opt. Express* **16**(20), 15514–15530 (2008).
51. J. G. Kim and H. Liu, "Investigation of biphasic tumor oxygen dynamics induced by hyperoxic gas intervention: the dynamic phantom approach," *Appl. Opt.* **47**(2), 242–252 (2008).
52. G. Peskir, "On the diffusion coefficient: The Einstein relation and beyond," *Stoch. Models* **19**(3), 383–405 (2003).
53. S. O. Rice, "Mathematical analysis of random noise," in *Noise and Stochastic Processes*, N. Wax, ed. (Dover, New York, 1954), p. 133.
54. S. A. Walker, S. Fantini, and E. Gratton, "Effect of index of refraction mismatch on the recovery of optical properties of cylindrical inhomogeneities in an infinite turbid medium," *Proc. SPIE* **2979**, 219–225 (1997).
55. X. Li, "Fluorescence and diffusive wave diffraction tomographic probes in turbid media," Ph.D. dissertation (University of Pennsylvania, 1998).

56. EngineeringToolBox, "Unit Converter with the most Common Units," http://www.engineeringtoolbox.com/unit-converter-d_185.html.
57. R. Choe, "Diffuse optical tomography and spectroscopy of breast cancer and fetal brain," Ph.D. dissertation (University of Pennsylvania, 2005).
58. S. A. Prahl, "Optical properties spectra," <http://omlc.ogi.edu/spectra/index.html>.
59. H. J. van Staveren, C. J. M. Moes, J. van Marie, S. A. Prahl, and M. J. C. van Gemert, "Light scattering in Intralipid-10% in the wavelength range of 400-1100 nm," *Appl. Opt.* **30**(31), 4507-4514 (1991).
60. S. Fantini, M. A. Franceschini, J. B. Fishkin, B. Barbieri, and E. Gratton, "Quantitative determination of the absorption spectra of chromophores in strongly scattering media: a light-emitting-diode based technique," *Appl. Opt.* **33**(22), 5204-5213 (1994).
61. S. Spichtig, R. Hornung, D. W. Brown, D. Haensse, and M. Wolf, "Multifrequency frequency-domain spectrometer for tissue analysis," *Rev. Sci. Instrum.* **80**(2), 024301 (2009).
62. D. Hueber, S. Fantini, A. Cerussi, and B. Barbieri, "New optical probe designs for absolute (self-calibrating) NIR tissue hemoglobin measurements," *Proc. SPIE* **3597**, 618-631 (1999).

1. Introduction

Near-infrared (NIR) light has been recently employed in the noninvasive acquisition of blood flow information from deep tissues (up to several centimeters), which is referred to as NIR Diffuse Correlation Spectroscopy (DCS) [1-4] or Diffuse Wave Spectroscopy (DWS) [5,6]. DCS measures relative change of tissue blood flow (rBF) which has been extensively validated in various tissues through comparisons with laser Doppler flowmetry (LDF) [7], Doppler ultrasound [8,9], power Doppler ultrasound [10,11], Xenon-CT [12], fluorescent microsphere measurement [13], arterial spin labeled magnetic resonance imaging (ASL-MRI) [14,15], and to literatures [1,4,16-18]. DCS also provides a blood flow index for comparisons of longitudinal measurements and inter-subject variations [11,13,19,20]. The probing depth of NIR DCS (several centimeters) is significantly larger than those (several millimeters) of similar optical modalities such as LDF [21-23], Doppler optical coherence tomography (DOCT) [24], photoacoustic tomography (PAT) [25], and optical micro-angiography (OMAG) [26]. DCS is primarily sensitive to microvasculature rather than large blood vessels (e.g., Doppler ultrasound measurement), and does not require radiation exposure (e.g., PET, Xenon-CT). Systems based on DCS provide portability, allowing for bedside monitoring utilizing short acquisition time (varying from 6.5 ms to several seconds) without expensive instrumentation [17,27-29]. Due to these features, usages of DCS expand continuously into new applications in various deep organs/tissues such as muscle [15,28,30-33], tumor [10,11,19,20,29,34-36] and brain [4,5,7-9,12-14,16,17,27,37-41].

The use of NIR light for deep tissue measurements stems from the exploitation of a spectral region (650-950 nm) wherein light absorption of the biological tissue is relatively low. When using NIR spectroscopy (NIRS) to detect optical properties of deep tissues, a pair of source and detector fibers is usually placed along the tissue surface with a distance of a few centimeters. NIR light generated by a laser emits into tissues through the source fiber and is detected by a photodetector through the detector fiber. Photon migration in tissue is now known to be a diffusive process [2,7]. During this migration, photons encounter absorption and, more commonly, scattering events. The probabilities of these events are described by an absorption coefficient, μ_a , and a reduced scattering coefficient, μ_s' , also referred to as the optical properties, intrinsic to the probed tissue volume. The penetration depth of NIR light in biological tissues is approximately half of the source-detector separation. NIR DCS flow measurements are accomplished by monitoring speckle fluctuations of photons emitted at the tissue surface. In non-muscular tissues moving red blood cells (RBC's) inside vessels are primarily responsible for these fluctuations [4,5,7-14,16,17,19,20,27,29,34-42], but complications such as tissue shearing and motion artifacts can arise for muscular tissues [28,32]. Blood flow indices and rBF can be calculated from the changes in the speckle patterns. Ensuing calculations of blood flow using DCS measurements include a dependence on the optical properties (μ_a and μ_s') and are thus potentially influenced by variations thereof (see the details in Section 2).

DCS is not inherently capable of measuring absolute values of absorption and scattering coefficients. Solutions to this issue have typically been approached using two general methods: optical property assumptions or optical property measurements with separate instrumentation. Some studies have chosen to use the values of μ_a and μ_s' from the literature [8,32], respective to the tissue type (e.g., brain or muscle), or assumed a constant μ_s' while examining changes in μ_a [13,30,40]. These assumptions may be susceptible to deviations in optical properties that occur transiently, longitudinally, due to subject differences or from differences in literatures. A few of the recent studies have employed hybrid instrumentation allowing for measurement of both sets of information to extract accurate blood flow [9,19,29,43]. However, a generalization of potential flow index errors due to the inaccurate estimation of optical properties has not been investigated for the DCS flow measurements. In addition to optical properties, another potential influence on DCS flow indices is determined by selection of the laser wavelength.

Our lab has recently built a hybrid instrument capable of the simultaneous measurement of absolute μ_a , μ_s' and flow indices at multiple wavelengths, through combining a commercial frequency-domain NIR tissue-oximeter, the Imagent (ISS, Inc., IL, USA) [44,45], and a custom-made NIR DCS flow-oximeter [31,33,41]. This newly developed hybrid instrument allows us to quantify the influences of optical properties on DCS flow indices measured at different wavelengths. In this study, homogeneous liquid phantoms with controlled variations of optical properties were created, attempting to isolate the influence of each optical property parameter (i.e., μ_a or μ_s') on DCS flow indices. The usage of tissue-like phantoms for instrument calibration and experimental validation of NIRS and DCS techniques is common [2,4,44–51]. In DCS measurements, the dynamic scatterer motions (typically microvasculature RBC's) are best modeled by Brownian diffusion as opposed to random ballistic flow, which has been determined empirically, but for reasons currently unknown [4,7,8,10,11,20,27,40]. An *effective* Brownian diffusion coefficient is calculated as the blood flow index when measuring in biological tissues and is usually distinct from the conventional Brownian diffusion coefficient predicted by Einstein [52]. However, when utilizing liquid phantoms with Intralipid particles to provide Brownian motion, the two diffusion coefficients are expected to be equivalent. Through this special case using liquid phantoms, DCS flow indices calculated using measured or assumed optical properties can be compared to the Einstein prediction (as a true flow index) for Brownian particles suspended in liquid. Measurement errors are then determined through these comparisons for DCS flow indices at different wavelengths.

Simultaneous measurements of optical properties and blood flow indices are essential for extracting accurate hemodynamic information in tissues with transient, longitudinal and inter-subject differences in optical properties. To this end, we show a clinical study using the hybrid instrument to accurately quantify tissue optical properties and blood flow indices in head and neck tumors. The measurement errors in tumor blood flow indices induced by potential inaccurate estimations of tissue optical properties are ultimately discussed and compared to the phantom study results to determine the *in vivo* applicability thereof.

2. Methods and materials

2.1. Diffuse correlation spectroscopy (DCS) for blood flow measurement

DCS flow indices are quantified by a dual-wavelength DCS system [31] with two long coherence length continuous-wave (CW) NIR laser sources at 785 and 830 nm (100 mW, Crystalaser, Inc., NV, USA). The DCS sources emit light alternately into the tissue via two multi-mode optical fibers bundled at the same location on the tissue surface (see Fig. 1a). Four detector fibers are tightly bundled and placed on the tissue surface at a distance of 1.5 cm away from the source fibers, and each is connected to a single photon-counting avalanche photodiode (APD) (PerkinElmer Inc., Canada). The outputs of 4 APDs are sent to a 4-channel

autocorrelator board (Correlator.com, NJ, USA) producing normalized light intensity temporal autocorrelation functions (g_2) which are averaged to improve the signal-noise-ratio. The averaged g_2 from DCS is related to the normalized electric field temporal autocorrelation function (g_1) through the following Siegert relation [53]:

$$g_2(\vec{r}, \tau) = 1 + \beta |g_1(\vec{r}, \tau)|^2 \quad (1)$$

where τ is the delay time, \vec{r} is the position vector, and β depends on laser stability and coherence length and the number of speckles detected.

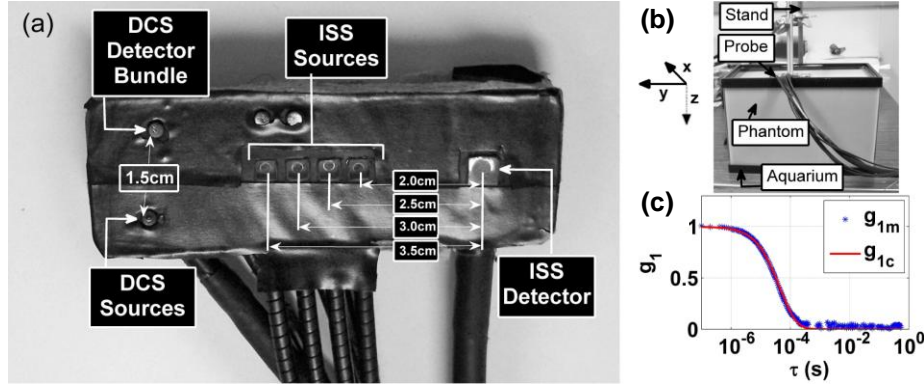


Fig. 1. (a) Hybrid fiber-optic probe comprised of: two DCS source fibers (785 and 830 nm) and four bundled DCS detector fibers separated by a distance of 1.5 cm; eight ISS source fibers (780 and 830 nm) and ISS detector fiber separated by distances of 2.0, 2.5, 3.0 and 3.5 cm (2 source fibers per separation distance). Note that two additional DCS detector fibers are shown, at 2.4 and 2.8 cm separations, but were not connected for this study. (b) Cartesian coordinates oriented for DCS source and detector (left) and liquid phantom setup (right) including: ~9.5 L glass aquarium (30.5 cm x 21.0 cm x 15.0 cm), hybrid optical probe and holder, and lab stand. (c) Typical correlation function fitting from a phantom experiment (μ_a (830 nm) = 0.05 cm^{-1} , μ_s' (830 nm) = 10 cm^{-1}) with g_1 derived from g_2 measurements (g_{1m}) using Eq. (1) and g_1 calculated (g_{1c}) using Eq. (3).

Scatterer motion is directly associated with the unnormalized electric field temporal autocorrelation function (G_1) which obeys a correlation diffusion equation, derived rigorously elsewhere [2,46] and defined as follows for homogeneous media using a CW source (steady state):

$$\left(D\nabla^2 - v\mu_a - \frac{1}{3}v\mu_s'k_0^2\alpha\langle\Delta r^2(\tau)\rangle \right) G_1(\vec{r}, \tau) = -vS(\vec{r}) \quad (2)$$

where $D = v / (3\mu_s')$ is the photon diffusion coefficient, v is the speed of light in the medium, k_0^2 is the wavenumber, $S(\vec{r})$ is the source light distribution, and $\langle\Delta r^2(\tau)\rangle$ is the mean-square displacement of scatterers in time τ . The position vector, \vec{r} , denotes a general vector from a source to a point of detection. Note that G_1 is the unnormalized version of g_1 , i.e., $g_1(\vec{r}, \tau) = G_1(\vec{r}, \tau) / G_1(\vec{r}, 0)$. Scatterer movement for particles undergoing Brownian motion results in $\langle\Delta r^2(\tau)\rangle = 6D_B\tau$, where D_B is the *effective* Brownian diffusion coefficient. An α (0–1) term is added to account for not all scatterers being dynamic and is defined as the ratio of moving scatterers to total scatterers. The combined term, αD_B , is referred to as the blood flow index in biological tissues and is commonly used to calculate the relative blood flow (compared to the baseline flow index before physiological changes). In contrast to tissue samples where scatterers may be static (e.g., organelle, mitochondria) or dynamic (moving

RBC), all scatterers in liquid phantom solutions (see Section 2.4) are considered dynamic with $\alpha \approx 1$ and the flow index is thus reported as simply D_B . The homogeneous CW solution to Eq. (2) for semi-infinite geometry is

$$G_1(\rho, \tau) = \frac{\nu S_0}{4\pi D} \left(\frac{\exp(-K(\tau)r_1)}{r_1} - \frac{\exp(-K(\tau)r_2)}{r_2} \right) \quad (3)$$

where ρ is the source-detector separation, S_0 is source intensity, $K^2(\tau) = 3\mu_a\mu_s' + \mu_s'^2 k_0^2 \alpha \langle \Delta r^2(\tau) \rangle$, $r_1 = [\rho^2 + (z - z_0)^2]^{1/2}$, $r_2 = [\rho^2 + (z + z_0 + 2z_b)^2]^{1/2}$, $z_0 = 1/\mu_s'$, $z_b = 2(1 + R_{eff})/3\mu_s'(1 - R_{eff})$, $R_{eff} = -1.440n^{-2} + 0.710n^{-1} + 0.668 + 0.0636n$ and $n \approx 1.33$ (for tissues and phantoms) [7,46,54,55]. The R_{eff} term accounts for the mismatch between the medium and the air indices of refraction with n being the ratio between them.

For semi-infinite geometry, the collimating laser source at $(0, 0, 0)$ and detector at $(\rho, 0, 0)$ are placed on the tissue surface with $z = 0$ (see Fig. 1b). This solution (Eq. (3)) involves an extrapolated zero boundary condition including an isotropic source at $z = z_0$ and negative isotropic imaging source at $z = -(z_0 + 2z_b)$. The position vector, \vec{r} , from Eq. (2) considers the point source at $(0, 0, z_0)$ and the negative imaging source at $(0, 0, -(z_0 + 2z_b))$. The superposition of solutions to these two sources using infinite geometry provides the resulting Eq. (3) where now the semi-infinite boundary is modeled by the scalar parameter, ρ . Further details can be found elsewhere [46,55].

Flow index calculations begin with using Eq. (1) to first determine the β . Using the g_2 data at earliest τ and letting $g_1 \approx 1$ (i.e., $g_1(\rho, 0) = G_1(\rho, 0)/G_1(\rho, 0) = 1$) lead to $\beta = g_2(\rho, \tau \approx 0) - 1$. Using DCS measured $g_2(\rho, \tau)$, calculated β and Eq. (1), $g_1(\rho, \tau)$ is calculated for all τ . Equation (3) is then used with the unknown parameter αD_B (flow index) to fit the g_1 derived from DCS measurements (see Fig. 1c). For a complete frame of DCS data acquisitions at two wavelengths, two flow indices are obtained sequentially.

2.2. Frequency-domain spatially resolved NIRS for tissue optical property measurement

Quantification of absolute μ_a and μ_s' is performed by a frequency-domain multi-distance spatially resolved spectroscopy, i.e., the Imagent. Two wavelengths (780 and 830 nm) of a four-wavelength (690, 750, 780 and 830 nm) Imagent system are chosen to match the DCS lasers available (785 and 830 nm). The Imagent emits sinusoidally modulated light into tissue through 8 optical fibers (4 per wavelength) placed at four pre-determined distances (2.0, 2.5, 3.0, and 3.5 cm) from a detector fiber bundle connected to a photomultiplier tube (PMT) (see Fig. 1a). Source light is modulated at 110 MHz resulting in detected AC, DC and Phase (ϕ) information from multiple distances. A simplified solution based on semi-infinite geometry for the photon diffusion equation exposes linear relationships between ϕ , logarithmic AC or logarithmic DC and spatial distances [44,45]. From the fitting slopes (S_{AC} , S_{DC} , S_ϕ) of the linear relationships μ_a and μ_s' can be extracted at each wavelength. Different source-detector separations generally provide measurements at different depths/regions based on diffusion theory [3]. However, the depth/regional difference has minimal effect on measurement of optical properties of homogeneous phantoms.

2.3. Brownian motion of spherical particles in liquid phantoms

As mentioned earlier, when using liquid phantoms with Intralipid particles to provide Brownian motion, the *effective* Brownian diffusion coefficient (flow index) measured by DCS is expected to be equivalent to the conventional Brownian diffusion coefficient predicted by Einstein [52]. In the present study, DCS flow indices are compared to Einstein diffusion

coefficients for the estimation of measurement errors. The Brownian diffusion coefficient as defined by the Einstein-Stokes formula for spherical particles in liquid is

$$D_B = \frac{k_B T}{6\pi R\eta} \quad (4)$$

where k_B is the Boltzmann constant, T is the phantom temperature, R is the radius of the spherical particles and η is the viscosity [52]. In order to obtain the temperature and viscosity parameters, a temperature sensor (Physitemp, NJ, USA) is attached near the optical probe and viscosity is measured using a viscometer (Brookfield, MA, USA). Viscosity is reported in units of cP (centipoise), where $1 \text{ cP} = 1 \text{ mPa}\cdot\text{s}$ (millipascal·second) = $0.001 \text{ kg}\cdot\text{m}^{-1}\cdot\text{s}^{-1}$ [56]. The radius of Intralipid particles is estimated as 196 nm (see Section 2.5).

2.4. Liquid phantoms with varied optical properties

Liquid phantoms are comprised of distilled water, India ink (Black India 44201, Higgins, MA, USA) and Intralipid (30%, Fresenius Kabi, Uppsala, Sweden). India ink is used to manipulate the absorption coefficient of the phantom, $\mu_a(\lambda)$, where λ is the laser source wavelength. India ink is first diluted to a 10% solution with distilled water. The 10% ink solution (instead of pure ink) is used to create phantoms. Intralipid provides particle Brownian motion and control of the reduced scattering coefficient of the phantom, $\mu_s'(\lambda)$. Setup of the liquid phantom is shown in Fig. 1b. A hybrid fiber-optic probe is placed on the surface of the liquid phantom solution contained inside a glass aquarium. A custom-made probe holder attached to a lab stand holds the probe at the center of the solution to simulate a semi-infinite geometry.

For creating phantoms with μ_a variation, a list of $\mu_a(\lambda)$ and a constant $\mu_s'(\lambda)$ are chosen (see details in Section 2.5). The $\mu_a(\lambda)$ and $\mu_s'(\lambda)$ of distilled water, 10% ink solution, and 30% Intralipid are first determined. These values in combination with titration equations provide the necessary volumes of water, ink and Intralipid to achieve desired phantom optical properties [57]. The subscripts “ink”, “Intralipid”, and “water” are used in this paper to denote 10% ink solution, 30% Intralipid, and distilled water, respectively. The $\mu_{a \text{ ink}}(\lambda)$ is derived from spectrometer (Beckman Coulter, CA, USA) measurements. Since the 10% ink solution is out of the measurable range of the spectrometer, further dilution is performed to get a 0.025% ink solution for spectrometer absorbance measurements. Absorbance measured from multiple 0.025% ink solution samples are averaged and converted to the $\mu_{a \text{ ink}}(\lambda)$ [57]. The $\mu_{a \text{ water}}(\lambda)$ is taken from the literature [58]. The $\mu_{a \text{ Intralipid}}(\lambda)$ is assumed to be equivalent to that of water. Distilled water and 10% ink solution are both assumed to have no contributions to the phantom $\mu_s'(\lambda)$, i.e., $\mu_{s' \text{ water}}(\lambda) = \mu_{s' \text{ ink}}(\lambda) = 0 \text{ cm}^{-1}$. The $\mu_s'(\lambda)$ of 10% Intralipid is calculated using a Mie theory approximation [59]. The theory and details including the Intralipid particle radius and refractive index were described in the original derivation [59] which has been extensively used for quantification of Intralipid-based liquid phantoms [2,7,57,60,61]. For 30% Intralipid used in this study, $\mu_{s' \text{ Intralipid}}(\lambda)$ is the $\mu_s'(\lambda)$ of 10% Intralipid multiplied by a factor of three [57].

2.5. Phantom experimental protocols and data analysis

μ_a variation. In this protocol, variation of μ_a was induced while maintaining a constant μ_s' . Thirteen steps were performed to cover μ_a (830 nm) from 0.05 to 0.20 cm^{-1} with a step size of 0.0125 cm^{-1} (i.e., μ_a (830 nm) = 0.05, 0.0625, 0.075, ..., 0.20 cm^{-1}) and μ_s' (830 nm) = 10 cm^{-1} . Prior to beginning the Imagent requires calibration to a phantom of known optical properties. During this process, corrections are made to account for the efficiency of optical coupling among the lasers/detector, optical fibers, and phantom [45,62]. The Imagent was calibrated to a liquid phantom of equivalent composition and optical properties at the midpoint (step 7) of the experimental range, i.e., μ_a (830 nm) = 0.125 cm^{-1} and μ_s' (830 nm) = 10 cm^{-1} . The combined probe was then placed upon a liquid phantom at the lowest optical

property step, i.e., μ_a (830 nm) = 0.05 cm⁻¹. For each of 13 steps the following actions were taken. Desired volume of ink solution was added to the liquid phantom, mixed, and allowed to stabilize for 10 minutes. Viscosity data was attained during this time by extracting three 500 μ l samples. The three samples were carefully taken from the left, right and middle of the solution (at the surface) to minimize spatial variations without submerging the pipette. Room light was then turned off and the experimental setup was covered with black plastic to reduce ambient light. Measurements were taken by the hybrid optical instrument and temperature sensor for a 5 minute interval.

μ_s' variation. Variation of μ_s' immediately followed the performing of μ_a variation experiments. Between experiments the phantom from μ_a variation was disposed of and replaced with a new initial phantom for μ_s' variation. The hybrid probe was cleaned with alcohol pads and repositioned on the surface of the second phantom for μ_s' variation study. Neither Imagent nor DCS were shut down between protocols. Variation of μ_s' was induced while maintaining a constant μ_a . A scattering range of μ_s' (830 nm) from 4 to 16 cm⁻¹ with a step size of 1 cm⁻¹ (i.e., μ_s' (830 nm) = 4, 5, 6, ..., 16 cm⁻¹) and μ_a (830 nm) = 0.125 cm⁻¹ was performed over thirteen steps. The volume of Intralipid required to increase μ_s' as desired could potentially reduce μ_a as well as influence the level of probe submersion. To remedy the first difficulty, ink was added with the Intralipid to maintain the μ_a of the phantom. For the second, an equivalent amount of phantom solution was removed after being mixed at each step. Viscosity, temperature and hybrid optical measurements were taken similarly to those during μ_a variation.

Data analysis and presentation. Each 5 minute interval measurement involves post calculations of interval averages of μ_a and μ_s' at each wavelength along with the temperature, sample average of viscosity, and three diffusion coefficients (D_B 's). Data between intervals (i.e., adding/taking solution, stirring) are excluded from data analysis. The μ_a and μ_s' are measured by Imagent using the spatially resolved (slope) method (see Section 2.2) and averaged over the 5 minute interval. The averaged μ_a and μ_s' are then used as known parameters in fitting DCS measured g_2 's using Eq. (1) and (3) to produce two distinct DCS D_B 's, which are distinguished with subscripts describing the optical property values used for calculation of D_B . The first DCS D_B (D_{B-mid}) is calculated with the averaged μ_a and μ_s' measured from the middle interval, i.e., μ_a (830 nm) = 0.125 cm⁻¹ and μ_s' (830 nm) = 10 cm⁻¹, serving as the diffusion coefficient ignorant of optical property variation. Using the constant μ_a and μ_s' from the middle interval results in overestimations of μ_a and μ_s' during early intervals and underestimations at later intervals, thus causing errors in calculation of flow indices. The second DCS D_B ($D_{B-dynamic}$) is calculated using the averaged μ_a and μ_s' measured from the corresponding interval, providing the best evaluations of DCS flow indices. These DCS D_B calculations are repeated for both sets of wavelengths. The optical properties from the Imagent measurements at 830 and 780 nm are used in calculations of DCS D_B 's at 830 and 785 nm, respectively. The influence of wavelength mismatch (5 nm) between 780 and 785 nm is considered to be minor. The third D_B ($D_{B-Einstein}$) is calculated using Eq. (4) with the estimated particle radius, interval averaged temperature and three sample averaged viscosity. The estimated particle radius of 196 nm is determined to exhibit the least errors between the measured DCS flow indices ($D_{B-dynamic}$) and calculated $D_{B-Einstein}$ at the calibration point (step 7). This estimation falls within the range of Intralipid particle size reported in the literatures [2,59].

Measurement errors are characterized by calculating percentage errors between the measured values and predictions. P-values from Student t-tests are included for comparisons of measurement errors and the criterion for significance is $p < 0.05$. Results are presented in figures and tables to visualize measurement variations, differences between expected and obtained values, and the optical property influences on DCS flow indices. Data are depicted as mean \pm standard deviation (SD) in tables and SD is illustrated by error bars in figures.

2.6. *In vivo* quantification of head and neck tumor hemodynamics

The possible errors of assuming constant optical properties in calculation of flow indices may be more readily visualized through analysis of real tissue measurements. In order to evaluate such influences in *in vivo* measurements, tissue hemodynamic properties of head and neck tumors in 10 patients were measured using a hybrid optical instrument similar to that in the phantom study. Institutional review board (IRB) approval was given by the University of Kentucky and consent forms were obtained before subject participation. Only subjects with Stage III-IVb Squamous Cell Carcinoma of the Head and Neck (SCCHN) were included. Neck lymph nodes measuring more than 1 cm and clinically thought to be involved by tumor were selected to study.

The Imagent used 690 and 830 nm source wavelengths whereas DCS used 785 and 854 nm lasers. Other wavelengths used for phantom studies were not available for the tumor study. Thus, data from 830 nm for Imagent and 854 nm for DCS are analyzed for this tumor study as these wavelengths provide the best match. By contrast, the second pair of wavelengths (785 nm versus 690 nm) is excluded for data analysis due to the significance of wavelength mismatch (95 nm). The Imagent source-detector separations used (2.0, 2.5, 3.0, and 3.5 cm) are identical to the phantom study. DCS utilized 3 detector fibers at 1.5, 2.4, and 2.8 cm separations from the two source fibers. The probe was held by hand and secured on the subjects in the center of the area identified as tumor node while tumor optical properties and DCS flow data were obtained for ~2 minutes. DCS data from the 2.8 cm separation are examined, comparable to the tissue region/depth probed by the Imagent. Using different sets of optical properties measured by the Imagent, four DCS flow indices for each of 10 subjects are calculated and then averaged over the 2-minute measurement interval. The μ_a and μ_s' are averaged over the measurement duration (2 minutes) for each subject and used in calculating the first DCS blood flow index ($\alpha D_{B-\text{dynamic}}$), which is considered as a true flow index. The minimum, mean and maximum μ_a and μ_s' over 10 subjects are determined and used for calculating the respective remaining three DCS blood flow indices ($\alpha D_{B-\text{min}}$, $\alpha D_{B-\text{mean}}$, and $\alpha D_{B-\text{max}}$ respectively) for comparisons with the true flow index ($\alpha D_{B-\text{dynamic}}$). Data in figures are presented by interval mean \pm SD, where SD is depicted by error bars.

3. Results

3.1. μ_a variation

In order to evaluate the influence of μ_a variation on flow indices, thirteen steps of liquid phantoms were performed to cover μ_a (830 nm) from 0.05 to 0.20 cm^{-1} with a step size of 0.0125 cm^{-1} while maintaining a constant μ_s' (830 nm) = 10 cm^{-1} . For each step/interval of measurements over 5 minutes, the means and SDs of viscosity (from three samples), temperature and calculated $D_{B-\text{Einstein}}$ are displayed as data sets (means) and error bars (SDs) in Fig. 2. $D_{B-\text{Einstein}}$ (see Fig. 2c) is calculated using the measured temperature (see Fig. 2b) per interval along with the associated viscosity (see Fig. 2a) and estimated particle radius (196 nm).

The interval means and SDs (error bars) of μ_a , μ_s' , $D_{B-\text{Einstein}}$, $D_{B-\text{mid}}$, and $D_{B-\text{dynamic}}$ throughout the 13 steps of μ_a variation are displayed in Fig. 3. The measured values of μ_a (see Figs. 3a and 3d) and μ_s' (see Figs. 3b and 3e) at two wavelengths by the Imagent are compared to predictions calculated using spectrometer and Mie theory for the evaluation of measurement errors, respectively. Two DCS flow indices ($D_{B-\text{mid}}$ and $D_{B-\text{dynamic}}$) are compared to the $D_{B-\text{Einstein}}$ (as a true flow index) for both wavelengths (see Figs. 3c and 3f). The $D_{B-\text{mid}}$ or $D_{B-\text{dynamic}}$ at each wavelength is calculated using the DCS measurement with averaged μ_a and μ_s' from the middle interval [μ_a (830 nm) = 0.125 cm^{-1} and μ_s' (830 nm) = 10 cm^{-1}] or from the corresponding interval.

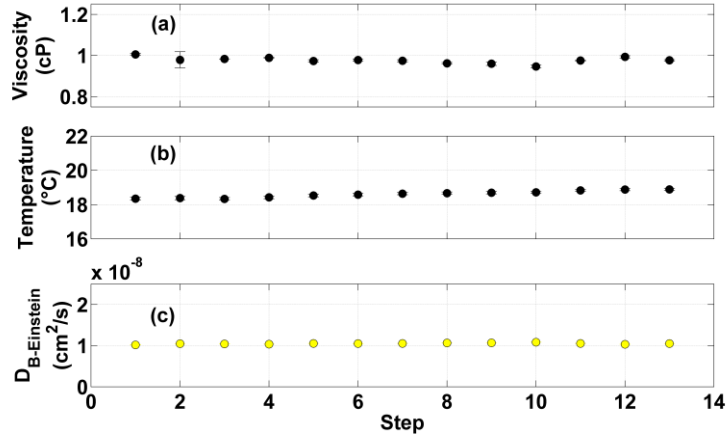


Fig. 2. Stability of Brownian motion ($D_{B-Einstein}$) during μ_a variation, depicted as means \pm SDs (as error bars). Viscosity (a) is averaged from three samples corresponding to each step; temperature (b) and $D_{B-Einstein}$ (c) are averaged respectively over 5-minute intervals.

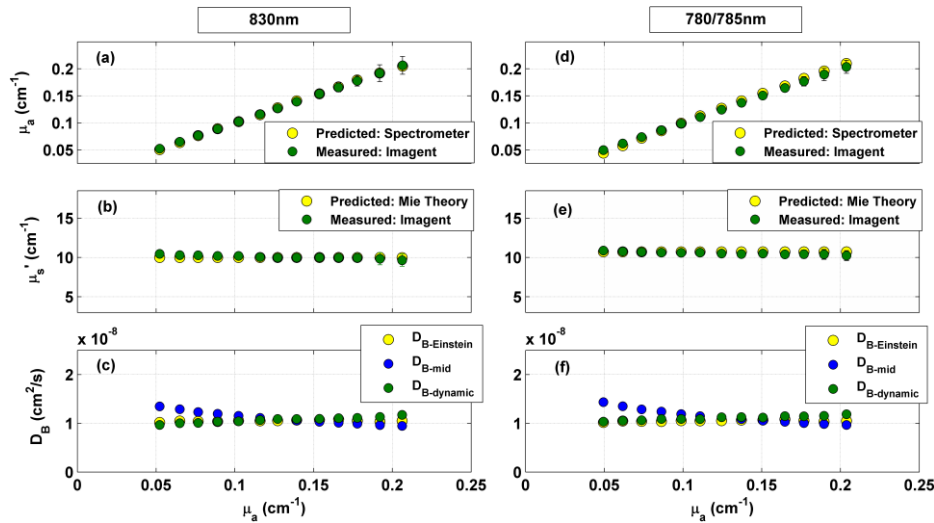


Fig. 3. Measured optical properties with calculated $D_{B-Einstein}$ and DCS flow indices during μ_a variation. Left panels represent measurements obtained by Imagent and DCS at 830 nm. Right panels show measurements from Imagent at 780 nm and DCS D_B calculations corresponding to 785 nm. All values shown, except predicted μ_a (a and d) and μ_s' (b and e), are interval means \pm SDs. Left panels: (a) μ_a (830 nm), (b) μ_s' (830 nm), and (c) $D_{B-Einstein}$ (830 nm), $D_{B-dynamic}$ (830 nm), D_{B-mid} (830 nm). Right panels: (d) μ_a (780 nm), (e) μ_s' (780 nm), and (f) $D_{B-Einstein}$ (785 nm), $D_{B-dynamic}$ (785 nm), D_{B-mid} (785 nm).

3.2. μ_s' variation

Similar to μ_a variation, a scattering range of μ_s' (830 nm) from 4 to 16 cm^{-1} with a step size of 1 cm^{-1} was performed over thirteen steps while maintaining a constant μ_a (830 nm) = 0.125 cm^{-1} . Results for μ_s' variation are plotted in a similar fashion as μ_a variation (see Section 3.1). The means and SDs (error bars) of viscosity (three samples), temperature and calculated $D_{B-Einstein}$ throughout μ_s' variation are shown in Fig. 4. The interval means and SDs of μ_a , μ_s' , $D_{B-Einstein}$, $D_{B-dynamic}$, and D_{B-mid} are displayed in Fig. 5.

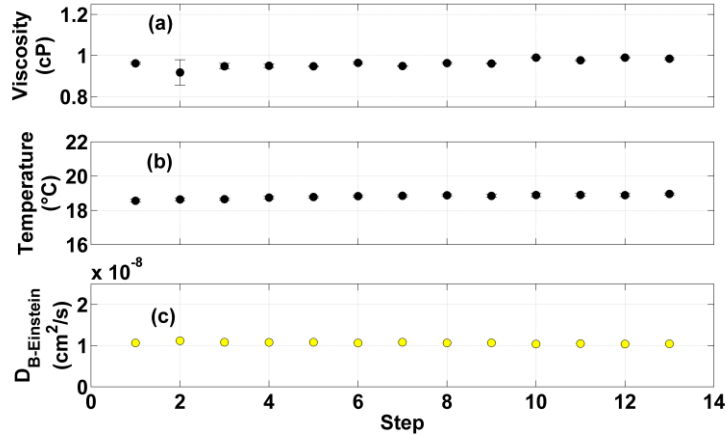


Fig. 4. Stability of Brownian motion ($D_{B-Einstein}$) during μ_s' variation, depicted as means \pm SDs (as error bars). Viscosity (a) is averaged from three samples corresponding to each step; temperature (b) and $D_{B-Einstein}$ (c) are averaged respectively over 5-minute intervals.

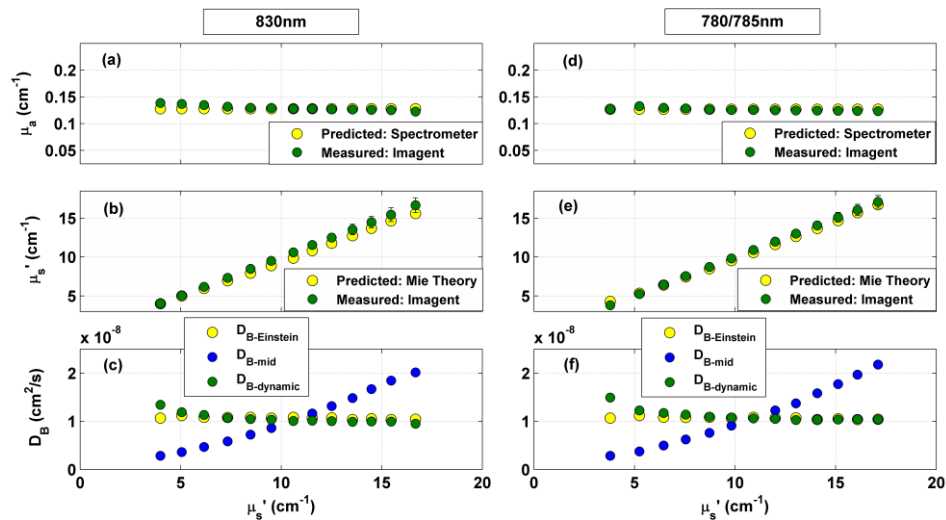


Fig. 5. Measured optical properties with calculated $D_{B-Einstein}$ and flow indices during μ_s' variation. Left panels represent measurements obtained by Imagent and DCS at 830 nm. Right panels show measurements from Imagent at 780 nm and DCS D_B calculations corresponding to 785 nm. All values shown, except predicted μ_a (a and d) and μ_s' (b and e), are interval means \pm SDs. Left panels: (a) μ_a (830 nm), (b) μ_s' (830 nm), and (c) $D_{B-Einstein}$ (830 nm), $D_{B-dynamic}$ (830 nm), D_{B-mid} (830 nm). Right panels: (d) μ_a (780 nm), (e) μ_s' (780 nm), and (f) $D_{B-Einstein}$ (785 nm), $D_{B-dynamic}$ (785 nm), D_{B-mid} (785 nm).

3.3. Quantification of μ_a and μ_s' influences on flow indices

Influence of μ_a and μ_s' variations on $D_{B-Einstein}$. Table 1 lists the means \pm SDs and coefficients of variation (CVs) for viscosity, temperature, and $D_{B-Einstein}$ over the entire range of μ_a and μ_s' variations, calculated based on the data shown in Figs. 2 and 4. The CV is defined as a percentage of SD/mean, indicating the variation of the mean values over steps. The CVs of temperature, viscosity, and $D_{B-Einstein}$ are less than 2.2%, indicating the minor influences of μ_a and μ_s' variations on these variables. The $D_{B-Einstein}$ is thus used as a true flow index to evaluate the DCS flow measurement errors.

Table 1. Mean \pm SD and CV of viscosity, temperature and $D_{B-Einstein}$

Variables	μ_a variation		μ_s' variation	
	Mean \pm SD	CV	Mean \pm SD	CV
Viscosity (cP)	0.98 \pm 0.02	1.54%	0.96 \pm 0.02	2.12%
Temperature ($^{\circ}$ C)	18.61 \pm 0.20	1.05%	18.80 \pm 0.12	0.64%
$D_{B-Einstein}$ (cm^2/s)	1.05E-08 \pm 1.65E-10	1.57%	1.07E-08 \pm 2.25E-10	2.11%

Mean measurement errors in μ_a , μ_s' and DCS flow indices. Table 2 lists the means \pm SDs of absolute percentage errors in measurements of μ_a , μ_s' , and DCS flow indices ($D_{B-dynamic}$ and D_{B-mid}) over the entire range of μ_a and μ_s' variations, calculated based on the data shown in Figs. 3 and 5. Absolute percentage error is defined as $(|Estimate-True|/True) \times 100\%$. For μ_a and μ_s' , the Imagent measured values are considered estimates while the spectrometer and Mie theory, respectively, are used as true values. For flow indices, $D_{B-dynamic}$ and D_{B-mid} are considered estimates and $D_{B-Einstein}$ as true. The measurement errors for μ_a , μ_s' , and $D_{B-dynamic}$ are small, averaging less than $\sim 7\%$, whereas those of D_{B-mid} are found to be larger, averaging up to 12.89% and 49.63% for μ_a and μ_s' variations, respectively. The influences of μ_s' variation can be seen to produce greater percentage errors on flow indices than those of μ_a variation. In Table 2, mean measurement errors between wavelengths are also compared using 2-sample unequal variance, two-tailed t-tests with significant differences considered for p-value < 0.05 and denoted with * prefix. Significant differences in mean measurement errors between wavelengths are found in μ_a ($p = 0.01$) during μ_a variation and in μ_s' ($p = 0.04$) during μ_s' variation. These differences between wavelengths are most likely associated with the intrinsic feature of the instrument (Imagent) in detection accuracy at different wavelengths. No significant differences in mean measurement errors between wavelengths are found for both $D_{B-dynamic}$ and D_{B-mid} .

Table 2. Imagent/DCS measurement percentage errors at 780/785 nm (upper line) and 830/830 nm (lower line)

Variables		μ_a variation (Absolute % Error)		μ_s' variation (Absolute % Error)	
		Mean \pm SD	p-value	Mean \pm SD	p-value
μ_a	780 nm	3.39 \pm 3.07	*0.01	1.86 \pm 1.15	0.23
	830 nm	0.84 \pm 0.95		2.86 \pm 2.69	
μ_s'	780 nm	1.93 \pm 1.23	0.54	3.14 \pm 2.66	*0.04
	830 nm	1.60 \pm 1.50		5.29 \pm 2.27	
$D_{B-dynamic}$	785 nm	5.52 \pm 3.69	0.28	5.84 \pm 10.73	0.83
	830 nm	4.02 \pm 3.30		6.58 \pm 6.16	
D_{B-mid}	785 nm	12.89 \pm 12.00	0.64	49.63 \pm 31.51	0.81
	830 nm	10.89 \pm 8.99		46.76 \pm 27.44	

*p-values < 0.05 **Table 3. The p-values for comparisons of the mean measurement errors between $D_{B-dynamic}$ and D_{B-mid}**

$D_{B-dynamic}$ vs. D_{B-mid}	μ_a variation (p-value)	μ_s' variation (p-value)
785 nm	0.0525	*0.0003
830 nm	*0.0205	*0.0002

*p-values < 0.05 .

Table 3 provides p-value results for comparisons of the mean measurement errors of $D_{B-dynamic}$ and D_{B-mid} at two wavelengths during μ_a and μ_s' variations. It is apparent that there are significant (though it is borderline at 785 nm during μ_a variation) differences between the measuring ($D_{B-dynamic}$) and assuming (D_{B-mid}) variables; $D_{B-dynamic}$ is more accurate (with less measurement errors, see Table 2) than D_{B-mid} . The much lower p-values for μ_s' variation as

compared with those for μ_a variation again suggest μ_s' as a greater influence factor on DCS flow indices.

Influence of μ_a and μ_s' variations on DCS flow index. Visualization of the influence of optical property assumptions at both wavelengths is shown in Fig. 6, overlaying the results from both μ_a and μ_s' variations over 13 steps (see Figs. 3 and 5). The percentage errors for μ_a during μ_a variation and for μ_s' during μ_s' variation are defined as $[(\mu_a - \mu_a - \text{dynamic}) / \mu_a - \text{dynamic}] \times 100\%$ and $[(\mu_s' - \mu_s' - \text{dynamic}) / \mu_s' - \text{dynamic}] \times 100\%$, respectively. The subscripts “mid” and “dynamic” correspond to assumed constant (middle-interval) and dynamic optical properties. For both variations, the percentage D_B error between $D_{B-\text{mid}}$ and $D_{B-\text{dynamic}}$ for each interval is defined as $[(D_{B-\text{mid}} - D_{B-\text{dynamic}}) / D_{B-\text{dynamic}}] \times 100\%$. Larger estimation errors in optical properties (μ_a and μ_s') generate larger percentage D_B errors. Variations in μ_s' have a greater influence on percentage D_B errors compared to variations in μ_a . Trends in overestimation and underestimation of flow indices due to variations in μ_a or μ_s' are different. Overestimating and underestimating μ_a results in overestimating and underestimating flow indices, respectively, opposite of the trend for μ_s' . Data for both wavelengths are in good agreement and show only minor differences.

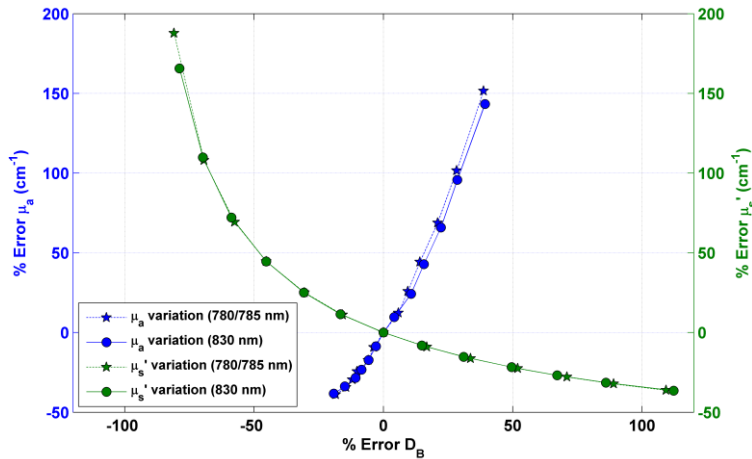


Fig. 6. Inaccurate estimations (percentage errors) of μ_a and μ_s' result in corresponding percentage D_B errors between $D_{B-\text{dynamic}}$ and $D_{B-\text{mid}}$ for both wavelengths.

3.4. Influence of tissue optical properties on head and neck tumor blood flow index

The means \pm SDs of measured tumor optical properties (μ_a and μ_s') and blood flow indices ($\alpha D_{B-\text{dynamic}}$, $\alpha D_{B-\text{min}}$, $\alpha D_{B-\text{mean}}$, and $\alpha D_{B-\text{max}}$) along with corresponding percentage errors for 10 patients with head and neck tumors are shown in Fig. 7. Patients are shown in order of increasing $\alpha D_{B-\text{dynamic}}$ (as true flow index), designated with a black line, for comparison of trend differences when using optical property assumptions (i.e., $\alpha D_{B-\text{min}}$, $\alpha D_{B-\text{mean}}$, and $\alpha D_{B-\text{max}}$). Note that the patient numbers represent indices to illustrate the trend rather than actual patient numbers corresponding to the measurement sequence. The mean optical properties over subjects are: μ_a (830 nm) = $0.12 \pm 0.03 \text{ cm}^{-1}$ and μ_s' (830 nm) = $7.80 \pm 2.64 \text{ cm}^{-1}$. Maximum and minimum optical properties out of all subjects at 830 nm are indicated using the red and blue dots, respectively, in Figs. 7a and 7b. DCS blood flow indices calculated using DCS data at 854 nm with different optical properties are represented in Fig. 7c. Without considering the tissue optical property influence, the trends of flow indices ($\alpha D_{B-\text{min}}$, $\alpha D_{B-\text{mean}}$, and $\alpha D_{B-\text{max}}$) are not the same as the true flow index ($\alpha D_{B-\text{dynamic}}$). Percentage αD_B errors are calculated between the $\alpha D_{B-\text{dynamic}}$ (true) and the estimated $\alpha D_{B-\text{min}}$, $\alpha D_{B-\text{mean}}$, and $\alpha D_{B-\text{max}}$.

Large ranges of percentage errors are found for αD_B estimates: $\alpha D_{B-\min}$ from -8.07 to 278.15% , $\alpha D_{B-\text{mean}}$ from -39.48 to 149.01% , and $\alpha D_{B-\text{max}}$ from -70.26 to 22.59% . The tendency to overestimate or underestimate the blood flow indices follow the same trends as shown for μ_s' variation in Fig. 6, supporting that μ_s' has a greater influence on DCS flow indices than μ_a .

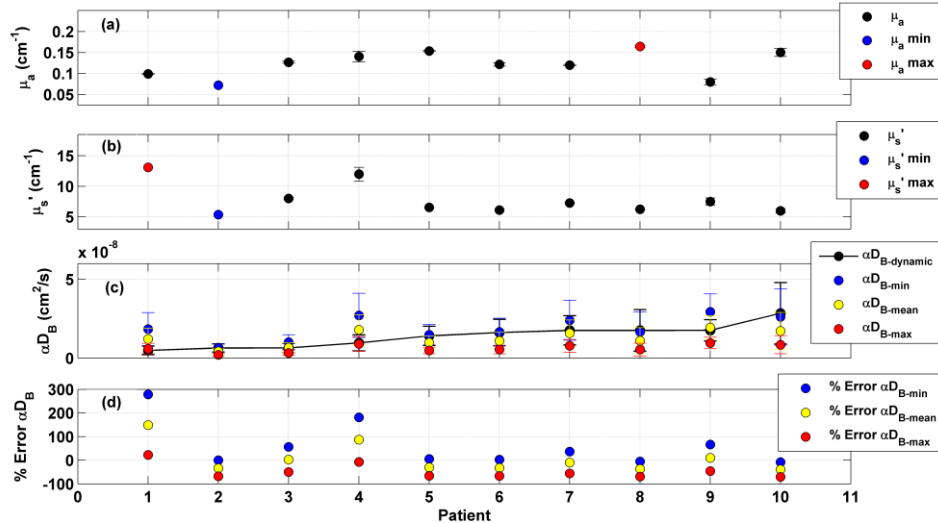


Fig. 7. Tumor optical properties measured by Imagent at 830 nm and flow indices measured by DCS at 854 nm using 830 nm optical properties. Data were obtained from tumor region for 10 subjects with head and neck tumors. All values, except percent errors (d), shown are means \pm SDs. (a) μ_a (830 nm), (b) μ_s' (830 nm), (c) $\alpha D_{B-\text{dynamic}}$ (854 nm), $\alpha D_{B-\text{min}}$ (854 nm), $\alpha D_{B-\text{mean}}$ (854 nm) and $\alpha D_{B-\text{max}}$ (854 nm), and (d) % Error $\alpha D_{B-\text{min}}$ (854 nm), % Error $\alpha D_{B-\text{mean}}$ (854 nm) and % Error $\alpha D_{B-\text{max}}$ (854 nm). Patients are listed in order of increasing $\alpha D_{B-\text{dynamic}}$ (854 nm).

4. Discussion and conclusions

4.1. μ_a and μ_s' variation influences on $D_{B-\text{Einstein}}$

The Einstein-Stokes formula calculation, Eq. (4), provides the Einstein diffuse coefficient ($D_{B-\text{Einstein}}$) for spherical particles moving in liquid phantoms. The $D_{B-\text{Einstein}}$ is determined by the temperature and viscosity of the liquid as well as the particle radius of Intralipid in the liquid phantoms. Only slight variations are exhibited in overall average temperature (CV < 1.1%), viscosity (CV < 2.2%), and $D_{B-\text{Einstein}}$ (CV < 2.2%) during both μ_a and μ_s' variations, as seen in Table 1 and Figs. 2 and 4. The particle radius of Intralipid should not change during both μ_a and μ_s' variations. The changes in temperature are likely due to room temperature increase over the ~ 4.5 hour experimental durations. These include contributions by heat from equipment in the confined room. The cause of small variations in viscosity is likely due to the measurement variations by the viscometer. With these small variations in temperature and viscosity, it is thus expected that the derived $D_{B-\text{Einstein}}$ from Eq. (4) is stable over the large variations of optical properties.

On the other hand, increases of μ_a (ink concentration) during μ_a variation are expected to have no contribution to $D_{B-\text{Einstein}}$, as ink provides no particle motion. Similarly, increases of μ_s' (Intralipid concentration) during μ_s' variation do not show significant influence on $D_{B-\text{Einstein}}$, which is expected as all scatterers (Intralipid particles) provide equivalent motion in liquid phantoms and the ratio of moving scatterers to all scatterers (α) remains unchanged ($\alpha = 1$). Due to the independence of optical properties and high stability throughout, $D_{B-\text{Einstein}}$ is considered reasonable as the true flow index for spherical particles moving in liquid phantoms.

4.2. Measurement errors of μ_a , μ_s' , and $D_{B\text{-dynamic}}$

In agreement with expectations, ink contributes only to increasing the absorption of the phantom during μ_a variation. Additions of equivalent amounts of ink per interval resulted in linear increases in μ_a for both Imagent wavelengths (see Figs. 3a and 3d). Only minimal variations occurred in μ_s' at both wavelengths during μ_a variation (see Figs. 3b and 3e). Calibration at the midpoint [μ_a (830 nm) = 0.125 cm⁻¹, μ_s' (830 nm) = 10 cm⁻¹] may influence the variation patterns seen in Imagent measurements. Intralipid contributes linearly to μ_s' increases, as expected, during μ_s' variation for both Imagent wavelengths (see Figs. 5b and 5e). The μ_a stayed relatively constant with minimal variations during μ_s' variation (see Figs. 5a and 5d). Measured μ_a and μ_s' during both experiments are consistent with predictions from spectrometer measurements and Mie theory, respectively. More specifically, the μ_s' measurement errors were less than 6% (see Table 2) for both experiments and wavelengths, which are comparable to those obtained from the literature using the Mie theory estimation (see Section 2.4) [59]. Overall, average measurement errors of μ_a and μ_s' were small during μ_a (< 4%) and μ_s' (< 6%) variations (see Table 2), which are in agreement with those found in previous studies using frequency-domain spatially resolved NIRS [44,45]. For μ_a variation, significant difference was found between measurement errors of μ_a at 780 and 830 nm. For μ_s' variation, there was significant difference between measurement errors of μ_s' at 780 and 830 nm. These differences are likely attributable to the intrinsic instrument (Imagent) feature in detection accuracy at separate wavelengths.

Average measurement errors for $D_{B\text{-dynamic}}$ (< 7%) compared to $D_{B\text{-Einstein}}$ at both wavelengths are similar to those obtained for optical properties (< 6%) during both experiments (see Table 2), suggesting the influence of optical properties on D_B .

4.3. Resulting D_B errors from optical property assumptions

When using assumed constant optical properties (i.e., middle-interval μ_a and μ_s') to calculate $D_{B\text{-mid}}$, mean $D_{B\text{-mid}}$ measurement errors during μ_a (~13%) and μ_s' (~50%) variations (see Tables 2 and 3) were significantly higher than those of $D_{B\text{-dynamic}}$ (~7%). It is evident that the influence of μ_s' on the DCS flow index is much greater than that of μ_a . This result is further supported by the great difference in p-values, where p-values during μ_s' variation are much less than p-values during μ_a variation (see Table 3). Also, looking at Fig. 6, the range of D_B percentage errors for inaccurate estimations of μ_s' is much wider than that for μ_a . This result is expected due to DCS flow indices being derived from light speckle fluctuations, originated from photon phase shifts by dynamic scatterers. Upon examination of the K^2 definition (see Eq. (3)), μ_s' should have a more significant influence than μ_a given the $\mu_s'^2$ term along with the much larger scattering over absorption (i.e., $\mu_s' \gg \mu_a$) in biological tissues and the liquid phantoms. No significant difference was found between wavelengths in $D_{B\text{-dynamic}}$ and $D_{B\text{-mid}}$ measurement errors during both experiments (see Table 2). This indicates that wavelength may not be a critical factor in determining the importance of optical property influence on D_B measurement, although further investigations using a large range of wavelengths are needed for making a solid conclusion. The trends of D_B estimation errors when using $D_{B\text{-mid}}$ were found to be different between the μ_a and μ_s' variations (see Figs. 3c, 3f, 5c, 5f and 6). For μ_a variation, overestimated or underestimated μ_a results in overestimated or underestimated D_B . By contrast, for μ_s' variation overestimated or underestimated μ_s' results in underestimated or overestimated D_B . Extreme examples of incorrect estimations of D_B can be seen in Fig. 6. Overestimation errors of μ_a up to ~+150% during μ_a variation resulted in percentage errors up to ~+40% and underestimation errors up to ~-40% resulted in percentage errors up to ~-20%. When overestimation errors of μ_s' reach up to ~+175% during μ_s' variation, D_B percentage errors were up to ~-80%. For underestimation errors of μ_s' up to ~-35%, D_B percentage errors

reach up to $\sim+110\%$. Note that these estimation errors in optical properties and resulting D_B may be affected by the selection of phantom properties for calibration.

4.4. *In vivo tumor study data in comparison to phantom study results*

In the tumor study, measured μ_a and μ_s' show large variations between subjects (see Figs. 7a and 7b). The range of variations, μ_a (830 nm) from 0.07 to 0.16 cm^{-1} and μ_s' (830 nm) from 5.35 to 13.1 cm^{-1} , is within the range studied using liquid phantoms. The influence of the μ_s' variations on flow indices was found to be greater than that of μ_a , supporting the phantom study results. This is exemplified by the trends shown in Fig. 7c. The overestimation of optical properties (using maximum μ_a and μ_s') leads to underestimation of DCS flow index ($\alpha D_{B-\text{max}}$) and underestimation (using minimum μ_a and μ_s') leads to overestimation of DCS flow index ($\alpha D_{B-\text{min}}$). These are in agreement with the trends of D_B estimation errors using inaccurate μ_s' in liquid phantoms (see Figs. 5c, 5f and 6). Percentage αD_B errors range greatly, from $\sim-70\%$ up to $\sim+280\%$, depending on optical properties assumed. Errors in flow indices (see Fig. 7d) produce an incorrect observation of trends in the αD_B magnitudes among patients (see Fig. 7c). It is evident that lack of consideration for optical property influences can lead to invalid results in similar studies.

4.5. *Conclusions*

The advent of DCS technology as a safe and quick alternative for measurement of blood flow in deep tissues has brought the need to further investigate potential errors, notably by the assumption of constant optical properties, μ_a and μ_s' . The flow index produced by DCS measurement is based on a solution to the correlation diffusion equation which includes parameters of μ_a and μ_s' . Utilizing a novel hybrid optical equipment setup, capable of measuring all three parameters of interest (i.e., flow index, μ_a , and μ_s'), with liquid phantom experimental protocols has made it possible to perform this investigation. The present study evaluates the influences of tissue optical properties on DCS flow indices through isolated variations of μ_a and μ_s' in liquid phantoms. It is found that the particle motions in liquid phantoms are not influenced by the variations in optical properties, and the usage of Einstein particle Brownian motion coefficient ($D_{B-\text{Einstein}}$) as true flow index is reasonable for comparison with DCS flow indices. During μ_a and μ_s' variations, μ_s' has a much greater influence on DCS flow indices than μ_a , regardless of the wavelengths used. Studies involving significant μ_a and μ_s' changes should concurrently measure flow index and optical properties for accurate extraction of blood flow information in tissue. The flow index errors resulted from the optical property assumptions in the tumor study elicit such need for concurrent monitoring of optical properties. Incorporation of laser sources at wavelengths beyond those tested in this study may be the subject of future investigation. The range of optical properties tested in the phantoms may also be extended to encompass a wider variety of tissues.

Acknowledgments

The authors would like to thank the University of Kentucky Research Foundation and NIH R01 CA149274 for funding support. We also thank Daniel Kameny, Jacqueline Sims, Karen Meekins, and Laura Reichel for their assistance in recruitment of patients.